

## In-flight Calibration and Data Reduction for the WISPR Instrument On-Board the PSP Mission

Phillip Hess<sup>1</sup> · Russell A. Howard<sup>1</sup> ·  
Guillermo Stenborg<sup>1</sup> · Mark Linton<sup>1</sup> ·  
Angelos Vourlidas<sup>2</sup> · Arnaud Thernisien<sup>1</sup> ·  
Robin Colaninno<sup>1</sup> · Nathan Rich<sup>1</sup> ·  
Dennis Wang<sup>1</sup> · Karl Battams<sup>1</sup> ·  
Natsuha Kuroda<sup>3,1</sup>

© Springer ●●●

---

✉ P. Hess  
phillip.hess@nrl.navy.mil  
R.A. Howard  
russell.howard1924@gmail.com  
G. Stenborg  
guillermo.stenborg@nrl.navy.mil  
M. Linton  
mark.linton@nrl.navy.mil  
A. Vourlidas  
angelos.vourlidas@jhuapl.edu  
A. Thernisien  
arnaud.thernisien@nrl.navy.mil  
R. Colaninno  
robin.colaninno@nrl.navy.mil  
N. Rich  
nathan.rich@nrl.navy.mil  
D. Wang  
dennis.wang@nrl.navy.mil  
K. Battams  
karl.battams@nrl.navy.mil  
N. Kuroda  
natsuha.kuroda.ctr.ja@nrl.navy.mil

<sup>1</sup> U.S. Naval Research Laboratory Washington, D.C.

<sup>2</sup> Johns Hopkins University Applied Physics Laboratory Laurel, MD

<sup>3</sup> University Corporation for Atmospheric Research (UCAR) Boulder, CO

**Abstract** We present the calibration status and data reduction methodology for the Wide Field Imager for Solar Probe (WISPR) on board the Parker Solar Probe (PSP) mission. In particular, we describe the process for converting a raw image, measured in digital numbers (DN), to a calibrated image, measured in mean solar brightness (MSB). We also discuss details of the on-board image processing including bias removal, the linearity of the electronics, pointing, geometric distortion, and photometric calibration using stellar measurements, and the characterization of vignetting and other instrumental artifacts. The analysis presented here is based on data from the first 4 WISPR orbits. As the PSP perihelia get progressively closer to the Sun and the WISPR concept of operation evolves to deal with the brighter scene, the calibration will likely need to be updated. Aging of the optics and the possibility of detector degradation may also occur. Hence, we consider the WISPR calibration as work in progress with updates reported as necessary.

**Keywords:** Instrumentation and Data Management

## 1. Introduction

The Parker Solar Probe (PSP; Fox *et al.* 2016) mission was launched on August 12, 2018, carrying three in-situ and one remote sensing instrument: the Wide-Field Imager for Solar Probe (WISPR; Vourlidas *et al.* 2016). The first PSP perihelion occurred on November 01, 2018, shortly after launch, and led to the first WISPR science observations and results on both solar transients and the F-corona (Howard *et al.*, 2019). With an orbital period of about 3 months, PSP has completed 6 orbits about the Sun so far, and WISPR has acquired observations on coronal mass ejections (CMEs) (Hess *et al.*, 2020; Wood *et al.*, 2020), streamer flows (Rouillard *et al.*, 2020), coronal rays (Poirier *et al.*, 2020) and even faint dust trails from an asteroid (Battams *et al.*, 2020).

Unlike past solar missions, the PSP payload does not observe continuously. Instead, science observing windows open during encounters—when PSP orbits within approximately 0.25 AU of the Sun. The first perihelion reached  $35.6 R_{\odot}$  from the solar surface and throughout the 24 orbits of the mission, seven gravity assists from Venus fly-bys will gradually reduce the perihelion to an unprecedented  $8.86 R_{\odot}$  from the solar surface.

The science data are stored on the spacecraft and relayed to Earth at the earliest possible contact after each perihelion. Some data are also being taken outside of encounters, but this may contain special observing campaigns and calibration images that may not always be useful for science.

This paper is a basic introduction to WISPR data, its calibration status, data level products and overall data reduction and aims to assist the science community in the analysis of the WISPR observations. We start with the instrument overview (Section 2) and proceed to describe the various levels of WISPR data products (Section 3). In Section 4, we describe the on-board processing, including the electronic gains used, detector linearity, bias subtraction, and compression. We present the pointing and geometric corrections in Section 5, photometric

**Table 1.** General Information of the two detectors that make up the WISPR instrument.

	WISPR-I	WISPR-O
Resolution	2048x1920	2048x1920
FOV	13.5° – 53.5°	50° – 108°
Pixel Size	0.0210° (75.6")	0.0285° (102.6")
Spectral Range	490nm-740nm	475nm-725nm
Approx. Exposure at 0.25 AU	4.75 sec	105 Sec
Approx. Exposure at 0.16 AU	2.56 sec	40 Sec
Cadence	7-45 Min.	15-50 Min.

calibration in Section 6, and vignetting and instrumental artifacts in Section 7. We summarise the various calibration steps in Section 8 and present our conclusions in Section 9.

## 2. The WISPR Instrument

The WISPR instrument consists of two telescopes, WISPR-Inner (hereafter WISPR-I) and WISPR-Outer (hereafter WISPR-O), observing the inner heliosphere in white-light. WISPR-I has a 40° angular Field-of-View (FOV), centered approximately 33.5° from Sun center. The WISPR-O 58° FOV is centered approximately 79° from Sun center. The two FOVs slightly overlap resulting in total radial elongation coverage of 95°. The two telescopes use identical Active Pixel Sensor (APS) detectors. Each detector is 2048x1920 pixels, with the first 10 rows and columns opaque to incoming light and used for bias derivation since WISPR lacks a shutter. A model rendering of the WISPR instrument is shown in Figure 1.

The WISPR telescopes are most similar to the heliospheric imagers of the Sun-Earth-Connection COronal and Heliospheric Investigation ( SECCHI/HI; Howard *et al.*, 2008) aboard the twin Solar Terrestrial Relations Observatory (STEREO; Kaiser *et al.* 2008) spacecraft. The STEREO spacecraft orbit at 1 au with a heliocentric variation of less than 10%. But the PSP is in a Sun-Venus elliptical orbit and hence its heliocentric distance changes rapidly, particularly during perihelion. Since the WISPR angular FOV is fixed, the instrument’s linear coverage of the corona/heliosphere varies proportionally to the spacecraft radial distance. This is a unique situation for a solar telescope and creates novel science opportunities (discussed in more detail in Vourlidas *et al.* 2016).

The orbit design presents a number of challenges for understanding and calibrating the WISPR data. As a result, the WISPR calibration will evolve and improve as more data become available. While this is true, to some extent, for any long-lived mission, it is especially true for a mission with so many unique aspects. This paper presents the current calibration status, but users of WISPR

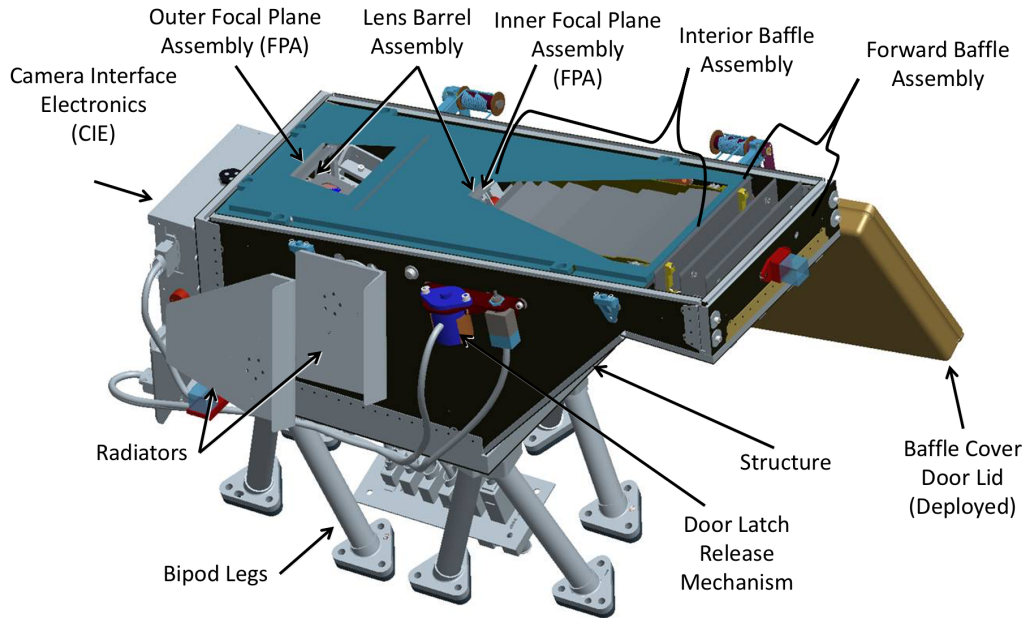


**Figure 1.** A rendering of the WISPR instrument.

data should be aware of the potential for changes in the calibrations and should make sure they use the most current data and calibrations.

### 3. Types of Observations and Data Levels

The synoptic program consists of full field observations from each detector at slightly varying cadence and exposure times dictated by the heliocentric distance of PSP. In addition, the observing program may include a number of special observing campaigns, mostly performed outside of the encounter window. Those campaigns include sub-fields, spacecraft rolls and off-points. To reduce telemetry, the images (including the synoptic ones) are binned on-board. The WISPR FITS header<sup>1</sup> contains information about the binning in the NBIN, NBIN1,

<sup>1</sup>See [WISPR Website](#) for a description of all the keywords in the WISPR FITS header.

and NBIN2 keywords, which indicate the number of original pixels combined in each binned pixel and the binning value in the x and y directions respectively. The majority of images are binned in 2x2 blocks, resulting in a 1024x960 image in detector coordinates. This binning is performed after the digitization of the image and unlike a CCD detector, this summing does not reduce the read-noise of the image but still has the benefit of reducing the file size so as to reduce the telemetry required for each image.

To increase the signal to noise ratio of the observations, the images are summed together, similarly to SECCHI/HI. The number of images in the sum used is given by the NSUMEXP keyword. The exposure of the summed image is the sum of the individual image exposures and is given by the XPOSURE keyword.

There are two additional observing modes. The first one is the Wave Turbulence Subfield (WTS), in which a small subfield along the sunward edge of the WISPR-I detector is used to image at a significantly higher cadence (usually 10-30 sec cadence). This observing mode is used for studies of small-scale density variability in the solar wind flow at cadences comparable (to the extent possible) to the in-situ measurements. This mode is only run for limited periods (15-min every hour) for a day or two at closest approach. WTS images are always single exposures and are never binned. The second observing mode is the Outer Swath program, comprising WISPR-O subfields extending along the full radial FOV and 5° in latitude. The images are recorded at cadence of about 24 minutes. The mode is usually run for a couple days before perihelion to provide imaging context of the structures that may be encountered by the spacecraft at perihelion.

The WISPR data are released in three data product levels. L1 data consists of FITS files in raw digital number (DN), a measure of the number of photoelectrons collected on the detector. The L1 processing consists of converting the telemetry packet data into a compressed image, then un-compressing the image and creating the FITS header using data from the downlinked image header, housekeeping information such as temperatures and statistics of the image itself. The spacecraft location and pointing information are also included in the header.

The L1 images are rectified, meaning rotated and flipped to ensure that the top of the image is oriented towards spacecraft north and the left edge of the image is on the sunward side. For nominal synoptic images, this means the top of the image will be in the same direction as solar north, though this will not be the case for images taken while the spacecraft is rolled. Apart from rectification and other processes performed on-board the spacecraft (see Section 4) no other corrections are applied to the L1 data.

L2 images have the correct pointing information and are photometrically calibrated in units of Mean Solar Brightness (MSB). The general equation for doing this is

$$I_{CAL} = \frac{C_f(I_{DN} - b)}{V_f T_{exp}} \quad (1)$$

where  $I_{CAL}$  represents the calibrated signal in MSB units,  $I_{DN}$  is the signal in DN of the digitized image,  $b$  is the bias of the detector,  $C_f$  is the calibration factor,  $V_f$  is the vignetting function of the lens and  $T_{exp}$  is the exposure time

of the image. The specific values for these quantities currently in use and how they were generated will be explained throughout the rest of this paper, as well as some other corrections that have been applied. After going through the L2 pipeline, the data are consistent in overall level, regardless of differences in the observing sequence (i.e. gain setting used or number of sums). Therefore, while the signal in a series of L1 images can change significantly due to changes in the observing sequence, the L2 pipeline has been designed to account for any effect caused by a change in the detector settings and create a stable data set.

The process for generating the L2 files normalizes for all the features unique to the individual observations, creating a photometrically stable data set. Changes in signal level between images are still common however, reflecting the varying height of the field of view.

L3 images are L2 images with the background subtracted to remove the smooth component of the F-corona and instrumental artifacts. They should contain only emission from K-corona structures (such as streamers and CMEs (Hess *et al.*, 2020; Wood *et al.*, 2020; Rouillard *et al.*, 2020) and discrete dust features such as comet/asteroidal dust trails (Battams *et al.*, 2020), and galactic and solar system objects. The L3 images are the primary products for science analysis. The generated backgrounds for each image are also released, as L2b files, in units of MSB. Background removal is generally necessary for white light observations of the corona and heliosphere as the signal from the dust (F-corona) is much higher than the signal from the coronal electrons. For 1 AU observations, the F-corona is stable on time-scales of years so the background can be determined empirically as the minimum brightness level over a set of month- or year-long time series, see Section 10 in Morrill *et al.* (2006) for the LASCO description. Unfortunately, this method is not applicable to WISPR due to the PSP mission profile. The background changes considerably from image to image due to the rapid movement and changing heliocentric distance of the spacecraft. In preparation for the mission, Stenborg and Howard (2017) developed a method to derive background estimates for individual images and demonstrated this method on SECCHI/HI1 images. The method, adapted for WISPR, is now used for the generation of the L3 data products. The details of the methodology of background estimation are described in (Stenborg, Hess, and Howard, 2021).

An example of the different processing levels for each telescope is shown in Figure 2. The images are from the first encounter. The dominance of the F-corona signal is obvious in the L1 and L2 images. The most apparent difference between L1 and L2 is the slight change in the shape of the F-corona, due to the vignetting correction (Section 7). This brings the F-corona shape in line with expectations from past observations (e.g., Stenborg, Howard, and Stauffer, 2018). In the L3 the F-corona is removed and both a streamer and a CME are now visible.

Another artifact of note in Figure 2 is the “letterbox” effect produced by the black bars at the top and bottom of the WISPR-O data. In the first orbit, a mask was applied to both the top and bottom 256 rows in most of the outer telescope images to reduce the file size and therefore the telemetry required for every image. It was later determined that the telemetry savings were rather small and it is no longer used.

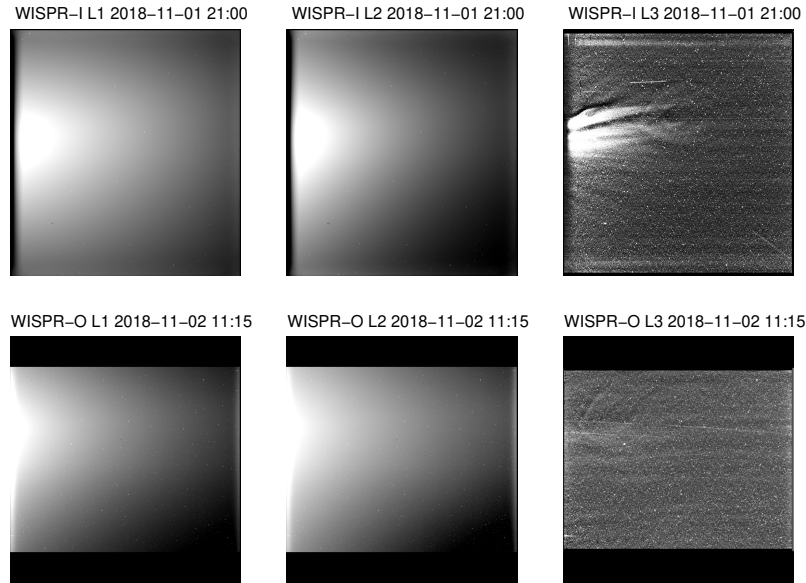


**Figure 2.** An example of L1, L2, and L3 versions of an image from both the WISPR-I (top) and WISPR-O (bottom) detectors in the first encounter. A faint CME is visible in the L3 files. The black bars in the WISPR-O data are a mask that was applied to reduce the file size.

Finally, there is one last data product, named CAL1. These are not science images, but are calibration and test images used to analyze the instrument. L1 versions of these files are publicly released, but processed or corrected versions are not, since they are not intended for science analysis.

### 3.1. Detector

To achieve such close perihelia, the PSP payload must satisfy strict mass, power and radiation requirements. It was realized early on that APS detectors offer the only viable imaging option, thanks to their low power and mass and high radiation tolerance compared to Charge-Coupled Devices (CCDs) (Korendyke *et al.*, 2013). APS detectors offer operational flexibility due to the existence of readout electronics below each pixel, which comes, however, with a reduction in active area. Although APS detectors are commonly used in the industry (i.e. in cellphone imagers), science-grade detectors for space applications are rare. The Solar Orbiter Heliospheric Imager (Howard *et al.*, 2020) project initiated the development of  $10\mu\text{m}$  APS detectors for heliophysics applications, joining a program that had been in development for some years (Janesick *et al.*, 2013). The WISPR detectors are part of the same fabrication run. The high functionality compared to CCDs greatly reduces the complexity of the camera control electronics. Unlike a CCD, which transfers the photo-electrons to a single output node to convert the charge into volts, APS detectors do the conversion at each pixel.

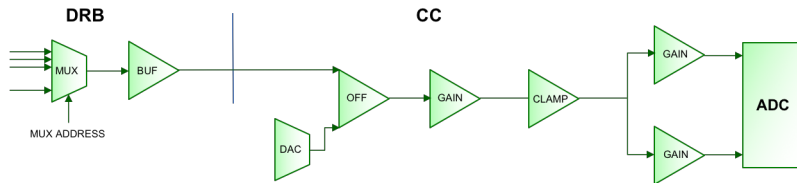


**Figure 3.** The Analog Signal Processing Chain. The analog processing is the off-chip processing leading to the digitization of the video signal. It is performed on two boards - the Digital Readout Board (DRB) located close to the detector inside the optical box and the Camera Card (CC) located outside. See the text for the description.

A metal-insulator-metal (MIM) capacitor was added to the pixel to increase the natural full well of the pixel from about 30 000 electrons to 120 000 electrons. This MIM capacitor can be turned on or off with the MIM select MOSFET switch. This MIM on/off capability, we call low/high gain because the number of electrons/DN is much higher in low gain than in high gain.

A preliminary calibration of the low gain data was performed on the ground, and we will provide an updated calibration of the low gain images by repeating many of the processes described throughout this paper once we have enough low gain images to allow for a thorough calibration across multiple orbits.

As the APS lacks a shutter which which to take a dark image, the first 10 rows and columns of the detectors have an opaque layer deposited on them. This opaque layer prevents photons from generating photo-electrons in the pixels and provides a dark signal with each image. This signal assists in the determination of the column-to-column variation, which is significant (see Section 4.3).

## 4. On-Board Processing

The on-board flight software applies a number of processing steps during image acquisition. The sequence of steps form part of the command upload for each observing program and they define the type of data that forms the L1 FITS file.

### 4.1. Gain Mode

WISPR can operate in two different gain modes, a low gain mode with a full well above 120,000 electrons and a high gain mode with a full well of over 30,000 electrons. In orbits 1-5 all science data was taken in high gain mode. Beginning in orbit 6, near perihelia the exposure time needed to resolve the F-corona without saturating in high gain mode would be below the minimum exposure time of 2.56 seconds, which is determined by the time to read out the detector. For this reason, low gain mode will be used more as we reach lower heights.

The video output is sent to the analog processing chain (see Sect. 3.1), where the signal is amplified. The amount of amplification is determined by ground command, to one of 14 levels. This allows the user to set the conversion of voltage to DN. The commanded value is returned in telemetry and is found in the GAINCMD keyword of the WISPR FITS header.

Originally gain 9 ( $2.134 e^-/DN$ ) was chosen as the default setting because it corresponded to a full well very close to detector saturation. After the analysis of the data from the first three encounters, we decided to change to gain setting 12 ( $2.716 e^-/DN$ ). While this has the downside of reducing the full well of an exposure from 16 383 DN to 12 860 DN, it ensures that the detector will saturate before the ADC, leading to the collection of the maximum possible amount of photo-electrons. The new setting was used during encounters 4 and 5. We are in the process of evaluating the quality of the images to decide whether to continue with gain mode 12.

## 4.2. Detector Linearity

Because of the frequently changing heights observed by WISPR as the mission progresses, it is necessary to frequently change the exposure time in order to optimize the measured intensity of the F-corona. However, with the first few changes in exposure time, running difference and running ratio images revealed artifacts immediately after a change. These artifacts were roughly the shape of the F-corona and can be seen in the middle column of Figure 4. Eventually it was determined that this was caused by a non-linearity of the detector that is more significant at higher observed intensities.

The magnitude of these artifacts is difficult to quantify as it varies based on the specific intensities observed before and after the exposure time changes, but in the ratios is typically on the order of 1-2%. In the individual images used to generate these ratios, we believe the deviation to be up to 5-6% at higher intensities, and lower throughout most of the well. We believe that this non-linearity at high signal levels is due to a leakage within the pixel (Janesick *et al.*, 2013).

Given the uncertainty on the photometric calibration (see Sect. 6), this 4-5% at the extreme end of the well would probably not be noticeable were WISPR observing at constant height with a single, typical exposure time. Even if just viewing un-corrected WISPR L2 images, the effect caused by the non-linearity at the changing of exposure times is extremely subtle.

The non-linearity becomes a major issue during the processing of the data to Level-3 by removing the F-corona. While we don't want to delve too deeply into the details of that process, which are explained in depth in Stenborg, Hess, and Howard (2021), some brief description is necessary to explain the significance of the non-linearity.

The first step of the process is to determine an individual background (which is released as the L2B product) for each L2 image, based on the separation of the different spatial scales of the K and F-coronae. The background subtracted images also instrumental artifacts, which can be at the same brightness level as the coronal features of interest. Therefore, to improve K-corona visibility, combining of background-subtracted images obtained over an extended period of time allows for the determination of an instrumental artifacts model. A hindrance of the time domain exploitation to create the artifact model is that pseudo-stationary features (*e.g.*, streamers) might be present in the resulting model and could then be subtracted out of the resulting L3. Therefore, combining multiple

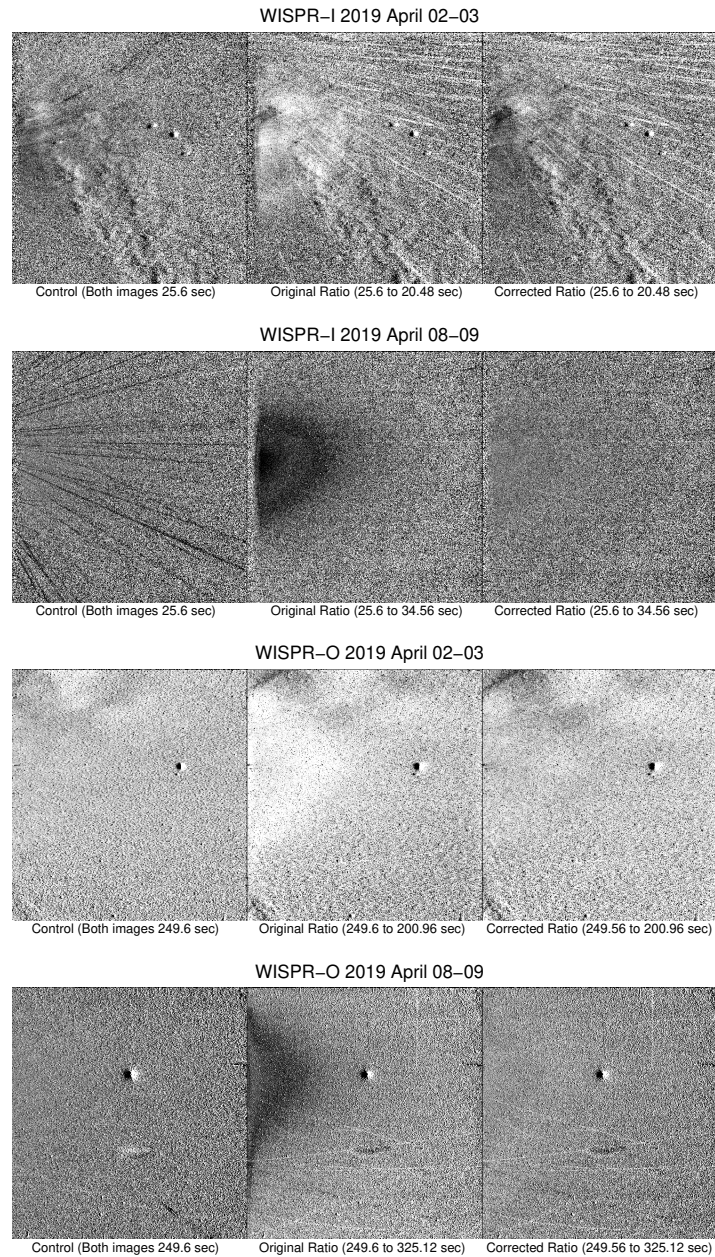


**Figure 4.** Examples of the artifacts found in ratio images at exposure time changes in both WISPR detectors. For each example, the image on the left represents a ratio image used as a control, chosen for having the same exposure time and as similar a cadence as possible as the images immediately before and after the exposure time change. The middle column is the original ratio image of the L2 data at the exposure time change, with no correction applied. The column on the right is the same ratio as the middle, but with the linearity correction applied to both of the original images.

orbits is desirable to create an artifact model (for details see Stenborg, Hess, and Howard, 2021).

A large scale artifact in L2 the signal of just a few percent due to a non-linearity issue negatively impacts the creation of the individual background for those images affected. This is because the effect is local, in the sense that it only occurs in a limited region and hence affects the smooth brightness profile expected. The background difference images of those images affected by this large-scale, local non-linearity effect might then exhibit a discontinuity (*i.e.*, an artifact) in the transition region where the non-linearity becomes significant (like those in the ratios of Figure 4). Because the K-corona brightness is orders of magnitude fainter than the F-corona for the vast majority of the observed heights in WISPR data (Koutchmy and Lamy, 1985), these artifacts, while small in absolute terms, can render the photometry of the K-corona structures in the L3 images completely unreliable.

For this reason it was determined that improving the linearity in the L2 files was necessary. Doing this without the benefit of a source with a known absolute intensity is difficult, and therefore the best we can do at this time is to create an empirical model that has been shown to reduce the artifacts in the L3 images.

Initially we attempted to determine this with a calibration test using an on-board LED with a fixed intensity. To test the linearity, the exposure time was varied on a  $256 \times 1920$  strip in WISPR-I from 5 to 140 seconds. The intensity profile of a given pixel was based on the proximity of that pixel to the LED. This provided a range of intensities covering the full well of the detector. A plot showing the performance of various pixels is shown in the left plot of Figure 5 as well as linear fits, based on the data with intensities below 6 000 DN.

The intensity in an APS detector is known to round off as it approaches saturation, so some deviation at the upper end of the well is expected. Given the limited data that reaches such a high intensity, this alone would not be a persistent problem in our observations. However, the data can be clearly seen to deviate from the linear fits throughout the upper half of the well, getting worse as the signal increases. The deviation as determined in the calibration test can be seen as a percentage in the black line of Figure 6.

Using this data to determine the correction did not completely remove the artifacts seen in Figure 4. This is because, without having a definitive understanding of what the observed intensity should be, based on the brightness of the LED in a given pixel and the remaining background signal also present in the detector, there was no way to specify what the 'correct' observation of electrons should have been. Instead of being able to measure our derived intensities from the proper value, a range of data had to be chosen to be fit with a linear profile. Deviation from this fit was considered the quantifiable non-linearity. As such, if the linear fit were performed on a different subset of intensities, the deviations derived would be slightly different.

Instead, the results from the linearity test were used as a starting point in an investigation of the science images taken at different exposures. To do this, a "control" ratio of two images taken at the same exposure was used to determine the proper ratio. Using a random process to alter the correction at different intensities in each image used to generate the ratio of combined exposures, the

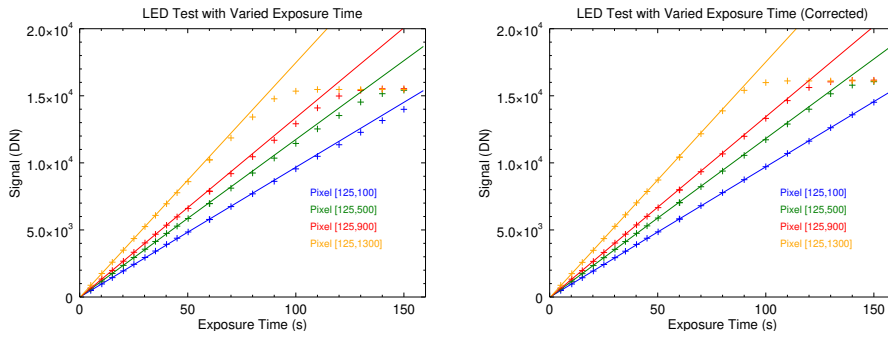


**Figure 5.** The detected signal in pixels at various locations in the strip used for the in-flight WISPR-I linearity calibration test, with the fits used to determine linearity. The left shows the raw data, while the figure on the right shows the data with the application of the determined linearity correction. The linear fits were carried out based on data below 6 000 DN.

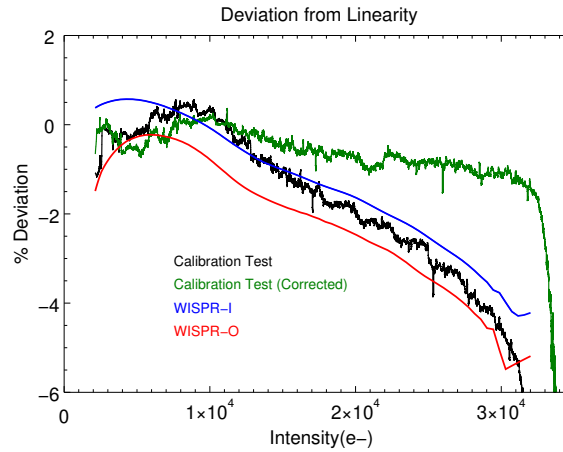


**Figure 6.** The black curve shows the % departure of linearity as a function of intensity, determined by an in-flight calibration test of WISPR-I. This was used as the starting point when determining the correction necessary to correct the images. The corrections for each detector are also shown for both WISPR-I (blue) and WISPR-O (red). The green shows the result of the linearity test with the correction applied. The intensity is given in electrons and is applicable at any gain setting. The % deviation represents the difference from the observed intensity to a linear intensity (i.e. a negative value indicates the signal in a given pixel is too low and must have the absolute value of the deviation added to make the signal linear.)

magnitudes of the resulting artifacts was minimized through an iterative process. This provided flatter, more consistent ratios and the correction derived this way could be applied to all the L2 data.

The application of this correction to the linearity test can be seen on the right half of Figure 5. While there is still some slight deviation from the linear profiles near saturation, the data is noticeably more linear. The residuals of this plot are also shown as the green line Figure 6. The maximum residual of this corrected data is about 1.5% before saturation takes hold, as opposed to being between 5-6% in the original data set. Because of the difficulty in directly comparing these

calibration images to science images, we think the result of the test done on science images with different exposures to be more reliable, so we consider this 1.5% remaining deviation from the calibration test to be an upper bound, and think that the resulting corrected data are likely to be linear to within 1%. The effect on the ratio images can be seen by comparing the images in the middle and right columns in Figure 4.

The resulting linearity correction curves are shown in Figure 6, as a function of electrons collected on the detector. The curves represent the difference between the observed signal at a given intensity and the expected linear signal. This means that negative values in Figure 6 represent the need for signal addition to the image. Neither curve reaches to 0 electrons or to detector saturation. We lack sufficient data in those regions to derive a correction.

WISPR-I and WISPR-O all have similar slopes to the non-linearity over most of the range of observed intensities, but differ in absolute magnitude. Because the detectors are identical, we would expect them to have similar non-linearity curves. The extra deviation in WISPR-O, which has exposures 8-10 times longer than WISPR-I, indicates the possibility of another contribution of lost electrons as a function of increasing exposure time, though we currently lack sufficient data to say this definitively. It is another reason why the original calibration test may not be reliable for determining the correction best used for science data, as the long exposure times needed to reach saturation with the LED may be introducing an additional effect. In fact, the WISPR-O correction at the higher end of the well looks much closer to the derived non-linearity from the calibration test. Because the calibration images at this end were generated at longer exposures more comparable to WISPR-O, this may be the cause of the extra non-linearity seen in the WISPR-I test.

The team considers the current correction a significant improvement over the original L2 data set. This correction is empirical in nature and as such can likely be improved. As more images are taken we will continue to examine the linearity and improve the correction if possible. It is also possible that, despite low gain data showing less deviation from linearity in pre-flight testing, more work will need to be done to derive a separate correction for low gain mode.

### 4.3. Bias Subtraction

The detector bias is uniform within a given column, but exhibits large column-to-column variability. Ground testing showed that the bias was temperature-dependent. Hence, the detector temperature is closely monitored and controlled. As shown in Figure 7, all images from both detectors in orbits 1 and 2 were taken at  $-71 \pm 0.3^\circ$ , with 98.7% of images being taken within  $\pm 0.2^\circ$  and 82.3% within  $\pm 0.1^\circ$ .

The temperature of the APS sensor is maintained by a Proportional-Integral-Derivative (PID) algorithm implemented in hardware. An aluminum cold strap conducts heat from the APS to a radiator located outside the WISPR Instrument Module (WIM). Each APS has its own radiator, which passively radiates the heat to deep space. The APS is attached to a molybdenum frame which is then attached to the cold strap. A foil heater is in the joint between the molybdenum

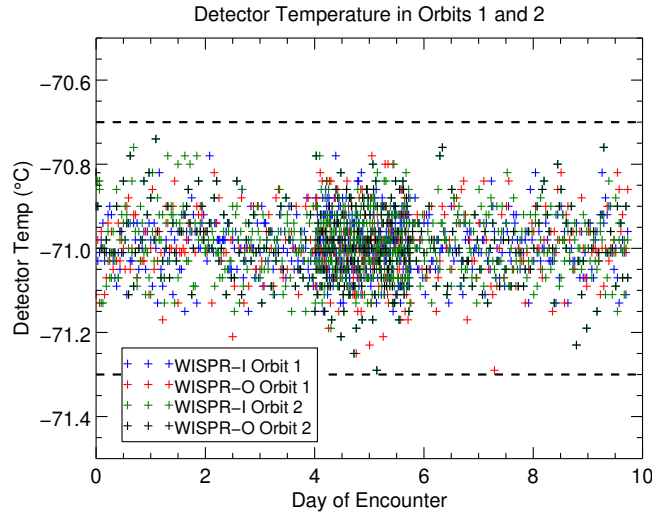


**Figure 7.** The detector temperature in both WISPR-I and WISPR-O for images taken during the first two encounters. The dashed lines at  $-71.3^\circ$  and  $-70.7^\circ$  represent the total range of temperatures.

frame and the cold strap. The temperature is set to be fixed around  $-71^\circ$ . The temperature is normally controlled to  $\pm 0.2^\circ$ . However, during the perihelia when the cadence is increased, more power dissipated on chip, which results in a control variation of  $\pm 0.4^\circ$  from the set point.

Bias subtraction can be performed either on-board or on the ground. For science images, bias subtraction is always performed on-board. This is because the column to column variation in the bias reduces significantly the effectiveness of the compression algorithm (see Section 4.4) and wastes telemetry.

The original approach was to use the signal in the masked pixels of each image to determine the bias for that image. However, the commissioning of the instrument revealed two drawbacks with this approach. The first was that, cosmic ray impacts on the masked pixels increased artificially the levels in the affected column, leading to negative values after the bias subtraction. The on-board processing cannot handle negative values (since these are nonphysical), the end result was 0 for the affected pixels. The second, related issue, was that the bias for a given column can only be subtracted off the entire column, masked rows included. This means that by the time the image was inspected on the ground, the masked pixels were zeroed and we had no way to determine what bias had actually been used.

Therefore, we decided on a different approach, wherein we take a dedicated bias image, usually twice daily, or whenever a sub-region is read out, and save that to send to ground for reference. This bias image is constructed using a 2.56 second exposure and averaging the masked pixels for each column. The bias image that is sent down to the ground is 64 rows due to a readout limitation on the detector limiting the size of a readout to multiples of 64. This revised

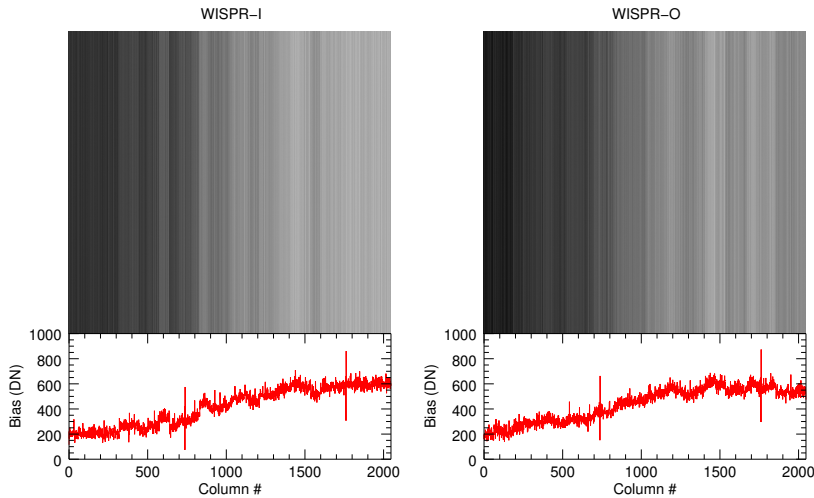


**Figure 8.** An example bias image from the WISPR-I (left; bias image from 2018-Nov-03 12:35 UT) and WISPR-O (right bias image from 2018-Nov-03 00:35). The line plots below each image show the signal level of the bias in each column. The images are uniform in the  $y$ -direction.

technique allows us to reconstruct both the level of bias subtraction in any image, and the evolution of bias with time. All synoptic science data taken with WISPR has used this approach to bias subtraction.

Subtracting the bias in this way significantly minimizes the risk of a cosmic ray impacting the bias by limiting the exposure to 2.56 seconds. If instead we were using the masked region of each individual image, the exposure time of that image would be the amount of time used to generate the bias. This means the masked pixels would be exposed for more than 10 to 100 times longer than in the current scheme for WISPR-I and WISPR-O, respectively, increasing the odds of a cosmic ray hit in the masked region by those same factors. Also, by saving and preserving the bias used in this way, in the event of a cosmic ray impact on the bias region we would at least be able to see the affected columns and take steps to mitigate the impact. To this point, we have yet to observe a cosmic ray hit in a bias image.

An example bias image from each detector, highlighting the clear column to column variation, is shown in Figure 8. These images are from the first encounter, but are representative of the bias images used throughout the orbit. The bias images are calibration data, and are not generally released. To show the relative stability of the bias value, we plot the mean of the bias images from WISPR-I throughout the first encounter in Figure 9.

We must determine the real bias offset for each image on the ground, which is a function of the residual offset for a single image and the number of summed images for the downlinked image and whether or not the image pixels were binned. We generally use the full image or 2x2 binned image. To do that we



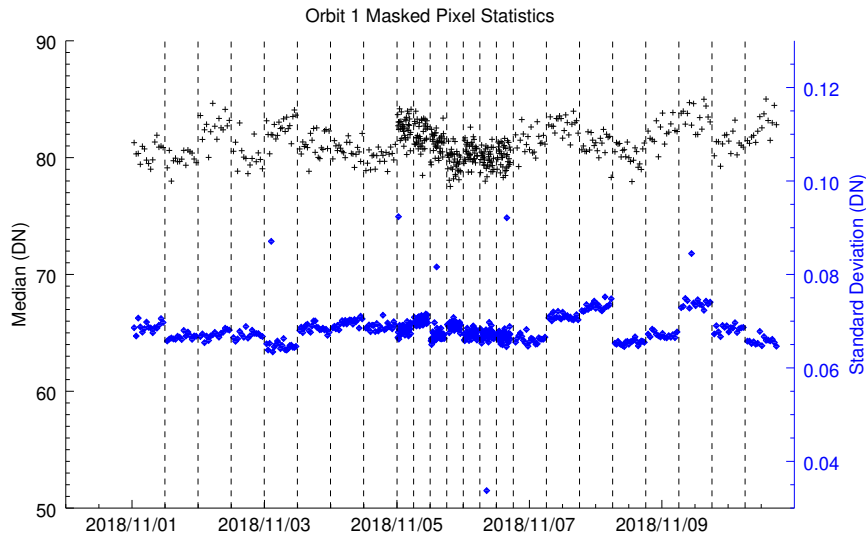


**Figure 10.** The median (black) of the signal remaining in the masked pixels after the bias is subtracted on-board. The blue diamonds are the standard deviation of the masked pixel signal. The vertical dashed lines indicate the timing of a change in bias image used.

had missing rows due to the excess bias resulting from these extra counts if the masked pixel region were being subtracted on-board instead of a pre-determined bias image.

#### 4.4. Compression

Because of the telemetry limitations of the mission, the compression is a vital component of the on-board processing to allow us to maximize the amount of data that can be taken in a given encounter. Although both lossless and lossy compression algorithms were implemented in the flight software, only lossless compression is currently being used.

The lossless compression starts by organizing the image into 64x64 pixel blocks. The size of the block requires the dimensions of the readout to be multiples of 64, so a full  $2048 \times 1920$  pixel image is reduced to a 32x30 set of 960 individual blocks. Each block is compressed separately. The lower left pixel of the block is the only pixel sent uncompressed. All of the other pixels in the block are differenced from their neighboring pixel, which is ultimately referenced to the lower left pixel. The 64x64 pixel block is divided up into 256 16-pixel segments. The difference per pixel in each segment is represented by  $n+1$  bits, where  $n$  is an integer and is set by the requirement that  $2^n$  be larger than the maximum absolute value of the difference per pixel in that segment.  $2^n$  is then added to each pixel in the segment so that the difference per pixel can be expressed as the positive number  $2^{n+1}$ . So, for example, if the difference

range was from +97 to -43, the number of bits needed per pixel to represent that segment would be +97 and the  $2^n$  value would be 128 ( $2^7$ ), so 7 bits would be needed to represent all the differences. Then all the differences in that segment would have 128 added to them. Thus the range of differences -127 to +127 is represented by 0 to 255. This process is repeated for every segment.

Because the compression is lossless, the accuracy of the compressed images is unaffected, regardless of the presence of any kind of intensity spike, like a cosmic ray or planetary transit. The presence of dust impacts (Szalay *et al.*, 2020) in particular has been a frequent issue, becoming more noticeable as the perihelia get closer to the Sun. These artifacts do impact the ability of the algorithm to reduce the size of the file that is ultimately sent to the ground. This is why we cannot determine the exact volume of our data before an orbit, but must instead do our best to estimate the compression performance as part of the planning for each encounter, so as to maximize the usage of our allocated data volume as much as possible without exceeding it.

## 5. Pointing and Geometric Distortion

We use the stellar field to perform the photometric calibration of the instrument, as has been done for both the LASCO C2 and C3 coronagraphs (Gardès, Lamy, and Llebaria, 2013; Colaninno and Howard, 2015; Morrill *et al.*, 2006; Thernisien *et al.*, 2006) and the SECCHI Heliospheric Imagers (Bewsher, Brown, and Eyles, 2012; Brown, Bewsher, and Eyles, 2009), but it is also useful for the pointing and geometric calibration. It transfers the pre-launch calibration to the same absolute photometric reference (i.e. the star field), but also permits the tracking of any degradation experienced in flight due to any cause.

The stellar calibration involves comparing the measured intensity of the stars to an analytic determination of what the brightness should be in physical units. This process is discussed in Section 6. Before this process can even begin, the optical parameters of the telescope must be accurately determined so that the stars can be reliably located and tracked through the FOV as the spacecraft moves in its orbit.

The optical parameters for each detector include the pointing of the detector boresight, the roll angle of each detector, as well as a geometric distortion function that models the warping and stretching of pixels, with those farther from the boresight being more significantly impacted. In SECCHI/HI, a linear distortion model was used, meaning that a single linear distortion coefficient was the term used to fit this distortion. For WISPR, a 6th order polynomial was chosen for the distortion model and was first estimated based on the Zemax<sup>2</sup> lens prescription, making the projected coordinate systems zenith polynomial (ZPN; Calabretta and Greisen 2002).

---

<sup>2</sup>[Zemax](#) is an optical modeling software.

### 5.1. Defining Coordinate Systems

There are a number of terms that go into determining the field of view of each detector, and these terms are all stored in the FITS header of an image. The instrument pointing and roll are provided by the instrument SPICE<sup>3</sup> kernel and stored in the CRVALi (where i=1 refers to the detector x coordinate and i=2 refers to the y) and PCi,j, which is a series of 4 keywords representing the transformation matrix of the roll and non-radial skew of the image frame. The boresight pointing location on the detector is provided in the CRPIXi keywords. The distortion model coefficients are provided within the PV1i.j keywords.

Two coordinate systems conforming to the World Coordinate System standard (Thompson, 2006) can be determined entirely based on information provided in the FITS header of an image. The default system is the Helioprojective Cartesian (HPC) coordinate system. In this system the x-y detector coordinates for each pixel can be converted into an elongation angle (x) and solar latitude (y) extended into the heliosphere. This is the coordinate system that is most useful for converting an observed interplanetary feature from detector coordinates into a physically meaningful depiction of its location. The keywords given above provide the values defining this coordinate system.

The second system is the Galactic Ecliptic Inertial (GEI) coordinate system. This system is used to represent the portion of the celestial sphere within a given WISPR image and allows the location of any pixel to be given in terms of Right Ascension (RA) and Declination (DEC). As such, this system is more useful for identifying stars or any other feature that is outside the Solar System. The keywords for the GEI system are the same as those for the HPC system, but with a capital letter “A” at the end (i.e. CRVALiA).

The two coordinate systems are each shown in Figure 11. While the two systems are obviously very different, they share a number of commonalities. The boresight pointing and the distortion are simply optical functions of the telescopes and will be the same regardless of the coordinate system in use. The GEI coordinates are more convenient for stellar calibration, but the determined information is applicable to HPC coordinates as well. Using the WCS routines built into the *SolarSoft* IDL libraries (Freeland and Handy, 1998) it is possible to quickly convert between pixel and physical coordinates for either coordinate system.

### 5.2. Distortion

To determine the accuracy of the pointing and distortion model, a test set of stars visible to WISPR had to be determined. Each WISPR telescope observes a large longitudinal range of the celestial sphere during each encounter. The declination of the FOV changes very little.

To determine the pointing and distortion parameters, we used the initial values measured on the ground as the starting point. With these values, we

---

<sup>3</sup>[SPICE](#) is an observation geometry system for space science missions.

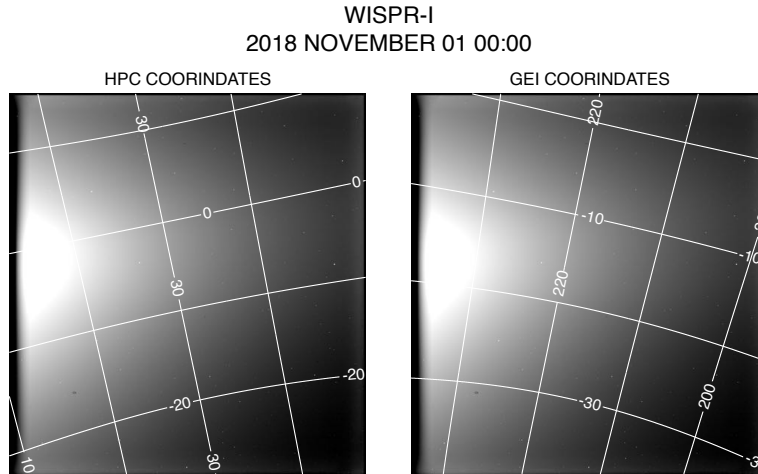


**Figure 11.** The different coordinate systems available in the WISPR header are represented with grids plotted on the same WISPR-I image from 2018 November 01 at 00:00 UT. The left panel shows the HPC coordinates and the GEI grid is on the right. The HPC system is roughly fixed throughout the mission, changing slightly from image to image. The GEI system will change more frequently based on the location of the spacecraft.

determined the total FOV in GEI coordinates in a particular image, using data from the first orbit. To find the visible stars in that image we searched the SIMBAD astronomical database (Wenger *et al.*, 2000) for stars with a magnitude below 7.5. We then converted the RA and DEC coordinates for the star from the database into a pixel location using the WCS\_GET\_PIXEL IDL routine and the projection information in the header.

We also applied a sigma filter to the image in order to remove the F-corona and isolate just the point sources, which we assumed to be almost entirely stars, although some could be the result of cosmic ray impacts. For the purposes of determining the location of the star, we were less interested in the observed brightness or point spread function and focused on the pixel location of the star's peak brightness. For each star selected from the catalog, we performed a 2-D Gaussian fit of a 10x10 pixel box, centered on the estimated pixel location from the catalog.

The distance between the expected and fitted position provides an estimate of the error of the optical parameters in the header. Using a least squares fitting routine, the distortion model coefficients that led to the smallest difference between the observed and expected stellar field was taken as the optical model of the instrument. These coefficients are included as the  $PV_{ij}$  variables in the headers. The distortion model is fixed, so these coefficients are the same in all WISPR L2 files.

The results of the star field identification from the minimized optical model in each telescope is shown in Figure 12. The location of stars in Figure 12 was determined by using the calculated distortion model to turn the RA and DEC coordinates from the SIMBAD catalog to pixel coordinates.

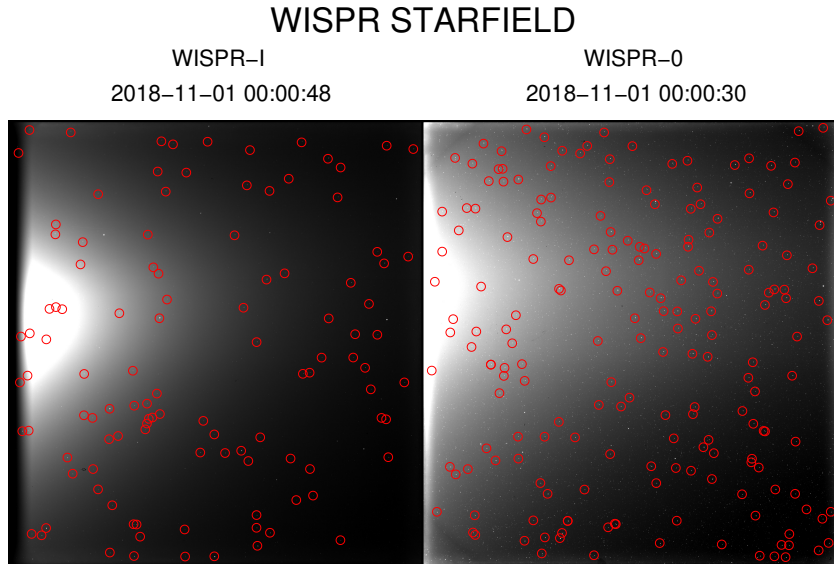


**Figure 12.** The circles represent the locations of all stars of magnitude 6 or less, given by the SIMBAD catalog, in sample WISPR L2 images from both WISPR telescopes. The locations of the stars are determined by using the WCS information reported in the L2 headers.

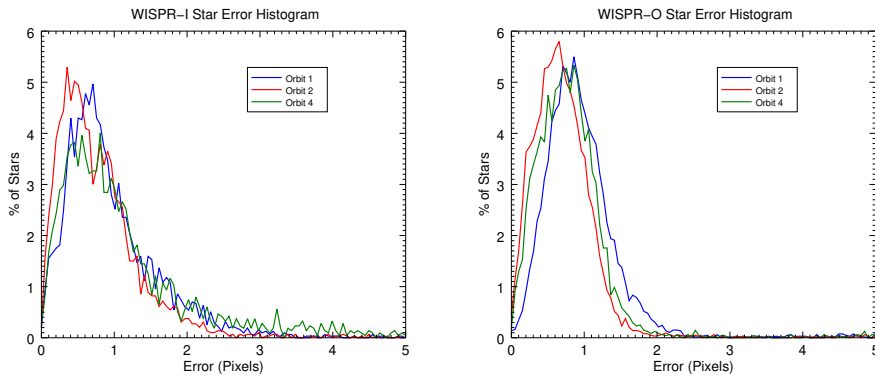


**Figure 13.** Histograms showing the distribution of stellar error for stars detected in images spanning orbits 1, 2 and 4 for the inner (left) and outer (right) telescopes.

To demonstrate both the accuracy of the distortion model and the stability of the pointing across the first four orbits, Figure 13 contains the histograms of the error, in absolute pixel distance, between the catalog pixel locations and the determined location of the stars from the image signal. These histograms were compiled by using images from the entire encounter, where the error in binned images was doubled to compare to un-binned images. The error in each histogram is both stable and largely concentrated to within a pixel in each orbit, so the distortion model is considered accurate. Subsequent orbits will continue

to be monitored for any noticeable drift in the star field relative to the current model.

## 6. Aperture Photometry

As has previously been discussed, the signal at the detector is measured in units of Digital Numbers (DNs), the digitization of the collected photo-electrons. After correcting for the bias and the linearity and dividing by the exposure time (in sec), the raw images are produced in units of DN/sec. Because the corona is an extended object (in comparison, say, to stars), this digital signal represents the coronal brightness ( $Wm^{-2}sr^{-1}pixel^{-1}$ ) over the bandpass of the instrument (e.g., Howard and DeForest, 2012). As the bandpass varies among different coronagraphs and heliospheric imagers, it is customary to express the coronal brightness relative to the average disk brightness ( $B_{\odot}$ ) over the *same* bandpass. The resulting physical unit is denoted as Mean Solar Brightness (MSB) or  $B/B_{\odot}$ . The MSB units can be translated to more common radiometry units by multiplying the values with the proper  $B_{\odot}$  for the given bandpass. Therefore, the emission of coronal features, expressed in MSB units, can be directly compared across different telescopes without further calibrations.

To convert the signal recorded in the WISPR detectors, from units of  $DN s^{-1}pix^{-1}$  into units of MSB:

$$Signal_{MSB} = C_f Signal_{DN}, \quad (3)$$

where the calibration factor,  $C_f$  ( $MSB/(DN sec^{-1}pixel^{-1})$ ), contains the effects of signal losses through the optical train, such as lens transmission and detector quantum efficiency. It depends on the gain setting,  $G_W$ , used during image acquisition. The WISPR electronics convert photo-electrons to DNs at the rate  $1/G_W$  where the units of  $G_W$  are  $electrons/DN$ . As for now, the vast majority of WISPR images were taken at high gain. The calibration factor is different between the WISPR-I and -O telescopes due to their slightly different bandpasses and throughput, as well as pixel size.

The telescope throughput is a combination of the lens transmission and detector quantum efficiency. Both were measured on the ground by the vendors and verified by the instrument team. The surface of one of the lenses was coated with a long pass filter and another lens had a short pass filter (WISPR-I has five lenses and WISPR-O has six (Vourlidas *et al.*, 2016)). The combination of these quantities as a function of wavelength is shown in Figure 14. It's possible that, due to degradation in the optics, this curve could change slightly as the mission progresses. This is one of the reasons the photometry must be continuously monitored and, if necessary, updated.

The solar spectrum is known, so integrating this over the curves shown in Figure 14 provided a high gain  $C_f$  value of  $3.93(5.78) \times 10^{-14} MSB/(DN s^{-1}pix^{-1})$  for WISPR-I (WISPR-O). These values were used to calibrate the images into MSB units at the beginning of the mission before the in-flight calibration was performed.

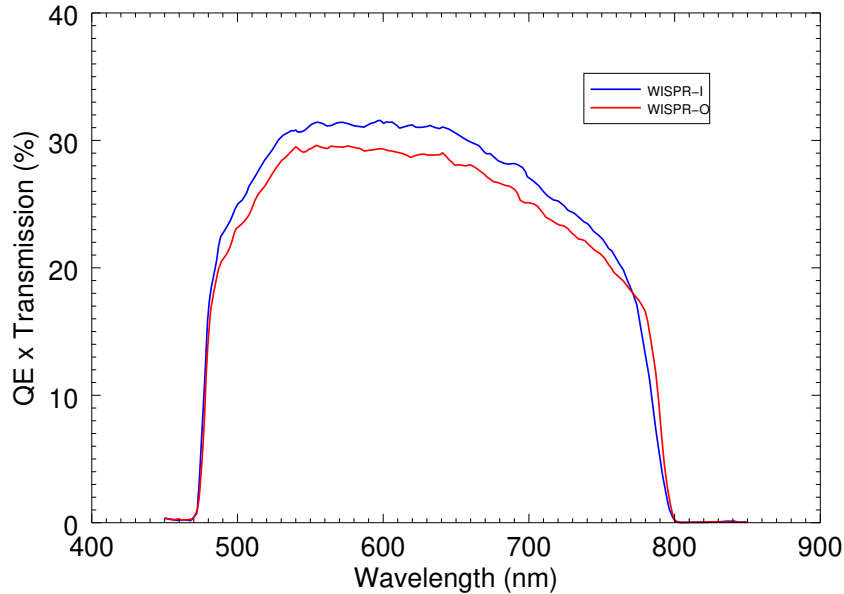


**Figure 14.** The transmission of each lens in the WISPR telescope multiplied by the quantum efficiency, representing the true efficiency of the lens brightness as a function of wavelength. This is used with the spectral information from the stars to perform the photometric calibration.

Having the component measurements is good, but it is always better to do an end-to-end verification of the response. Knowledge of the spectra of stars observed by the instrument can be used to independently determine  $C_f$ . This is done by using the star field from Section 5.2, as well as spectral information from the Pickles catalog (Pickles, 1997). A theoretical value for the total brightness of a star can be determined by integrating the catalog spectra over the instrument bandpass. This can then be compared to the observed brightness of the star to find  $C_f$ . Using enough stars, a statistically robust value of  $C_f$  can be determined.

To calculate the observed brightness of each star, aperture photometry has been performed on as many stars as possible across entire encounters for each detector, similar to processes carried out by Bewsher, Brown, and Eyles (2012) for SECCHI/HI1, Gardès, Lamy, and Llebaria (2013) and Colaninno and Howard (2015) for LASCO/C2 and Morrill *et al.* (2006) and Thernisien *et al.* (2006) for LASCO/C3. The images used for this study are corrected for the bias, the exposure time, the non-linearity and the vignetting (see Section 7).

The aperture photometry is performed by determining the stellar location in the same manner as described in the previous section. The integral of the total signal of the image inside a ring of a given pixel radius, centered on the expected star location, is found. This signal includes both the stellar signal and the background. To isolate the star, the background is determined by taking an annulus, defined by an inner and outer circle also centered on the expected star

location. The signal inside this annulus establishes the background signal. For the WISPR images, the stellar circle has a radius of 5 pixels, and the annulus is defined by radii of 7 and 10 pixels. The aperture photometry was performed with the IDL routine APER, a converted version of the FORTRAN photometry software DAOPHOT (Stetson, 1987).

The cadence of WISPR allows a star to be tracked across the field of view for multiple images. Despite the noise in the data that can cause great uncertainty in the brightness measurements, having multiple measurements for each star allows for a much more reliable measure for an individual star. The brightness for a given star is given as the median of the different measurements as it crosses the field of view. APER also provides an error of the intensity, and can remove stars that cannot be accurately measured, which could falsely influence the result. Using the outputs, we remove stars with with an error 50% or more of the total brightness.

Even with the extra reliability provided by having multiple images in which to track the star, there is still a great deal of noise in an individual star due, e.g., to multiple stars overlapping or variable stars. Fortunately, using a large enough sample of stars we can get a reliable photometric estimate of the detector response.

### 6.1. WISPR-I

The aperture photometry was performed on WISPR-I images from orbits 1, 2 and 4. Each of these orbits differed slightly from one other. In addition to changes in exposure times, the majority of images in orbits 1 and 4 were binned, while orbit 2 images were unbinned. Orbit 4 images, taken with gain setting 12, requires an additional factor to account for the different gain settings described in Section 4.1.

Table 2 shows the number of stars that were fit in each orbit, as well as the number of stars that both ultimately fit the error criteria and were matched in the Pickles catalog. The derived calibration factor is based on these stars. With more than 2000 stars tracked throughout the orbit, we have a large sample from each orbit.

Figure 15 shows the observed brightness plotted with the expected brightness for each of these orbits. As can be seen, the plots from each orbit are all stacked on top of each other, as long as the orbit 4 data is multiplied by 1.27 to match the differences in DN caused by the change in gain setting.

To further examine the orbit-to-orbit stability, we correlate the observed brightness of the same stars measured in each orbit. Comparing orbit 1 to orbit 2, the correlation coefficient between the common stars is 0.9756. The correlation between orbit 1 and 4 is 0.9764. These high correlations represent a trend in the stars common to the different orbits.

However, there still could be systematic changes in intensity from one orbit to the next that would not be revealed in this correlation. To test this, a linear fit to the signals from stars in two orbits was performed. In theory, if the stars were identical the slope of this fit would be 1. The slope of the orbit 1/2 fit is 0.9637. For the uncorrected orbit 4 data and orbit 1, the slope is 0.7844 due to

**Table 2.** For each WISPR-I orbit used for photometric calibration, this table shows the total number of stars tracked through the field of view (left) as well as the stars used for the calculation after removing those with large errors and checking the Pickles catalog for spectral information.

Orbit	Total Star Fits	Stars Used
1	5638	2295
2	8807	2294
4	6392	2725

the change in gain. If the 1.27 multiplier is applied to orbit 1, this slope becomes 0.9962.

Based on these values, the stellar signal appears consistent from orbit to orbit, regardless of the changes to observations. The slope of the data in Figure 15 corresponds to a  $C_f$  value of  $4.09 \times 10^{-14} B_{\odot} / (DN s^{-1} pix^{-1})$ . The image is multiplied by this number to convert the data into MSB units. For gain setting 12, this value becomes  $5.19 \times 10^{-14} B_{\odot} / (DN s^{-1} pix^{-1})$ . This value represents about a 4% increase in calibration from the value found on the ground.

Going forward, the photometric consistency will continue to be tested for more orbits to ensure that the values previously derived are correct and test for any potential degradation. We will also perform this same analysis on data taken in low gain mode once sufficient images are available. The ground derived calibration factors are  $2.49 \times 10^{-13} B_{\odot} / (DN s^{-1} pix^{-1})$  and  $3.43 \times 10^{-13} B_{\odot} / (DN s^{-1} pix^{-1})$  for WISPR-I and WISPR-O, respectively.

To further test the stability of the calibration factor and also estimate how much uncertainty there is on the stellar photometry, we can compare the calibration factor as determined by comparing each stellar observed brightness to its expected value. This gives us a range of calibration factors that can be studied as a population. The histogram shown in Figure 16 was calculated using the stars from orbits 1, 2, 4. Each orbit in which a star is observed separately is treated as a separate case for this histogram.

The distribution is normal enough to allow for the fitting of a Gaussian to the histogram. This fit has a centroid of  $3.95 \times 10^{-14} B_{\odot} / (DN s^{-1} pix^{-1})$ , and a width (standard deviation) of  $8.25 \times 10^{-15} B_{\odot} / (DN s^{-1} pix^{-1})$ . Taking this standard deviation as a measure of the error on the calibration factor, this represents a roughly  $\pm 20\%$  uncertainty on the calibration. This uncertainty is large, but we consider it an upper extreme and we hope to better constrain the calibration as more data is collected.

## 6.2. WISPR-O

The same aperture photometry process was carried out on WISPR-O, but only for the first orbit. This is because, while the total exposure time changed slightly

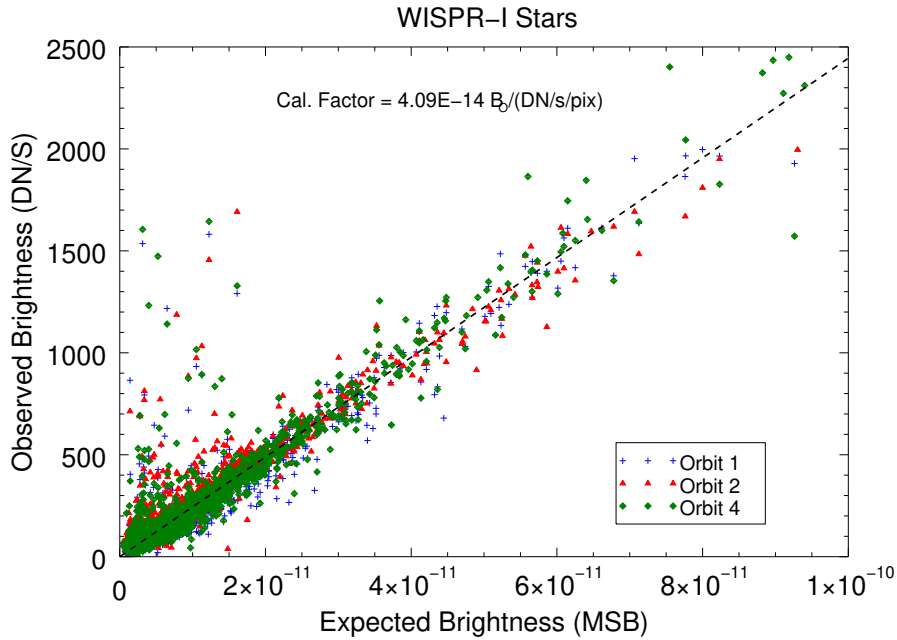


**Figure 15.** Each point in this plot represents a star that is tracked in the WISPR-I field of view in one of orbits 1, 2, and 4. The x-axis is the expected brightness in MSB of the star, based on spectral information from the Pickles catalog and the integral of the transmission curve from Figure 14. The y-axis is the brightness as measured during the stellar transit across the field of view, normalized for exposure time. The orbit 4 data has been multiplied by 1.27 to account for the change in gain setting. The dashed line represents the linear fit, providing a slope of  $4.09 \times 10^{-14} B_{\odot} / (DN s^{-1} pix^{-1})$ , representing the calibration factor to convert the measured intensity into physical units. Also note that the observed brightness, being a measured and more uncertain quantity, is plotted as the y-axis here. The conversion factor shown is therefore actually the inverse of the dashed line.

from orbit 1 to orbit 2, the number of sums that were used to generate each image was decreased from 12 to 5. This means the exposure time for an individual frame increased from 15 seconds to around 40 seconds (the exposure time changes throughout orbit 2, so this increase varies slightly). This increase in exposure time causes a much larger population of the stars to saturate, making it more difficult to obtain reliable statistics.

Figure 17 shows the stars from Orbit 1 in WISPR-O. A deviation from linearity is seen around  $200 DN s^{-1}$ , implying that stars at this level are beginning to reach saturation. This represents stars with a  $v_{mag}$  of roughly 6, or only 4% of the total sample.

As the detector saturates, the count rate becomes strongly non-linear and begins to fall off. Furthermore, on the lower end of the brightness scale, stars are dimming closer to the background and this introduces further ambiguity. Even focusing just on orbit 1 data, the fit in Figure 17, corresponding to a conversion factor of  $7.28 \times 10^{-14} B_{\odot} / (DN s^{-1} pix^{-1})$ , matches a limited range of brightnesses and creates doubt about the accuracy of this conversion factor. It's

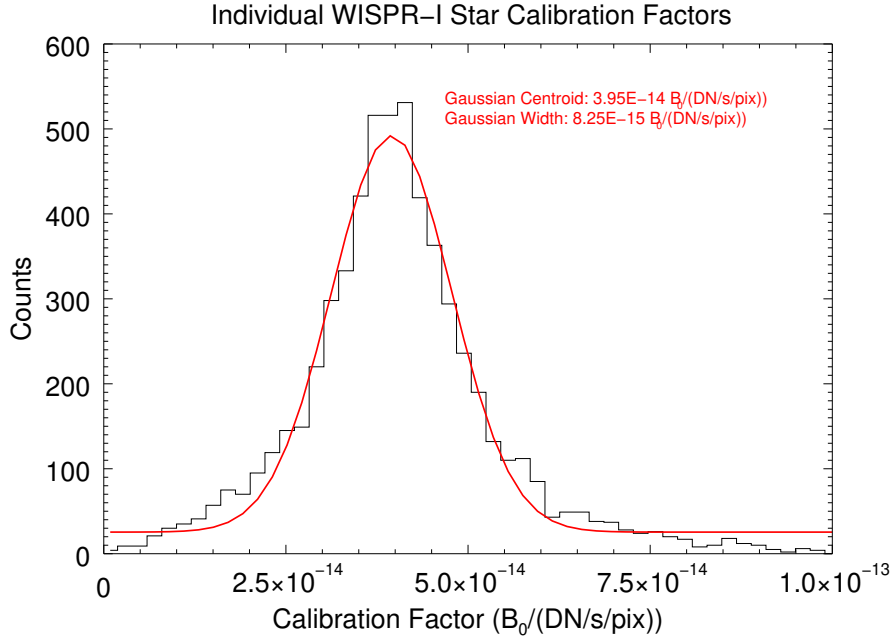


**Figure 16.** This histogram features every star (counts) from Figure 15, with a calibration factor determined individually by dividing the observed brightness by the expected brightness. The red line is a Gaussian fit of the data.

possible a more accurate linearity correction would cause more of these stars to fall on the line of the linear fit at higher magnitudes. However, the behavior of the APS as it approaches saturation and the distribution of stellar flux among multiple pixels makes it difficult to say when exactly saturation is beginning to kick in with the stars.

Because of the limited sample of measured brightness caused by the larger exposure times and increased pixel size in WISPR-O, there is more ambiguity in the WISPR-O fit (See Figure 15). Using the same histogram technique we applied to the stars from WISPR-I, Figure 18 shows the calibration factor derived by comparing the observed signal from each star to its expected brightness.

The Gaussian fit peaks at  $7.25 \times 10^{-14} B_{\odot} / (DN s^{-1} pix^{-1})$  with a half-width of  $1.57 \times 10^{-14} B_{\odot} / (DN s^{-1} pix^{-1})$ . This signifies a uncertainty of  $\sim 20\%$  on the calibration, comparable to WISPR-I. This does support that, despite the apparent visual deviation of brighter stars from the linear fit in Figure 17, the obtained calibration factor of  $7.28 \times 10^{-14}$  is reliable. Given that the field of view of the outer telescope is never expected to reach a height to necessitate using low gain mode, we don't expect to use it for WISPR-O. If that changes, a calibration for WISPR-O low gain will also have to be determined.

The histogram of Figure 18 shows that the majority of the stellar field used for calibration in WISPR-O fall along a steady slope in a roughly normal distribution. There are still obvious deviations at the brighter end of the stellar spectrum, and because the effects of the non-linearity discussed in Section 4.2

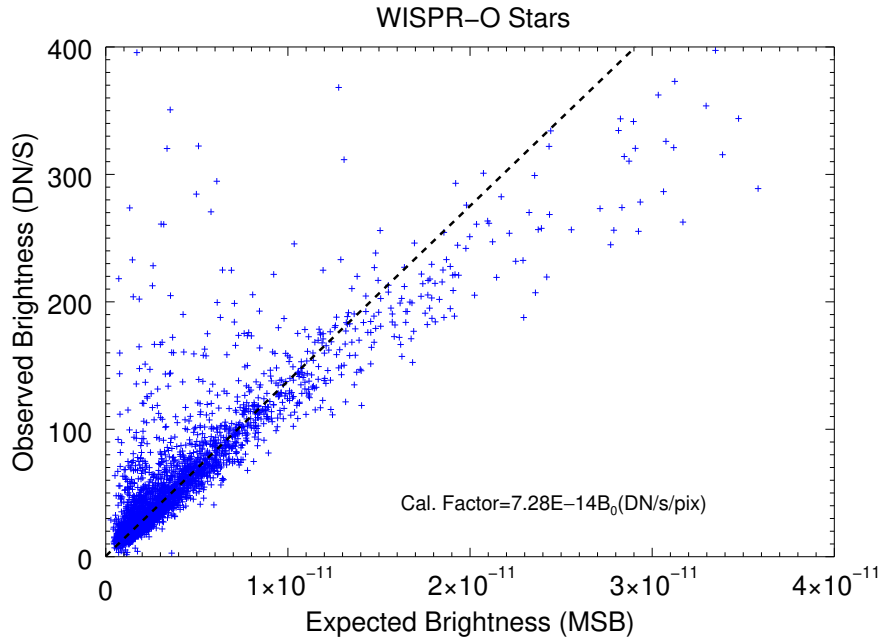


**Figure 17.** Each point in this plot represents a star that is tracked in the WISPR-O field of view in one of orbit 1. The x-axis is the expected brightness in MSB of the star, based on spectral information from the Pickles catalog and the integral of the transmission curve from Figure 14. The y-axis is the brightness as measured during the stellar transit across the field of view, normalized for exposure time. The orbit 4 data has been multiplied by 1.27 to account for the change in gain setting. The dashed line represents the linear fit, providing a slope of  $7.28 \times 10^{-14} B_{\odot} / (DN s^{-1} pix^{-1})$ , representing the calibration factor to convert the measured intensity into physical units. Also note that the observed brightness, being a measured and more uncertain quantity, is plotted as the y-axis here. The conversion factor shown is therefore actually the inverse of the dashed line.

cannot be entirely separated from the saturation of individual pixels within a star, it is certainly possible that an improvement to the linearity correction could cause more of these “saturated” stars to fall on the linear fit. Because of the combination of on-board binning and bias subtraction, pinning down the exact saturation point of a pixel cannot be done.

We will continue monitoring the linearity to see if this can be improved. Any improvement will almost certainly be restricted to only the highest portion of the well. Because the instrument is generally operated to keep the maximum F-corona signal approximately 25% below any potential saturation, there should be relatively few pixels in a given image that reach such intensities. Therefore, we believe the non-linearity correction currently in use will largely correct any issues in the F+K coronea intensities, even if an improvement that better fits the stars is eventually found. Should there be a particularly bright feature observed, the brightness and any derived density/mass therefrom may have to be considered to have a higher uncertainty.

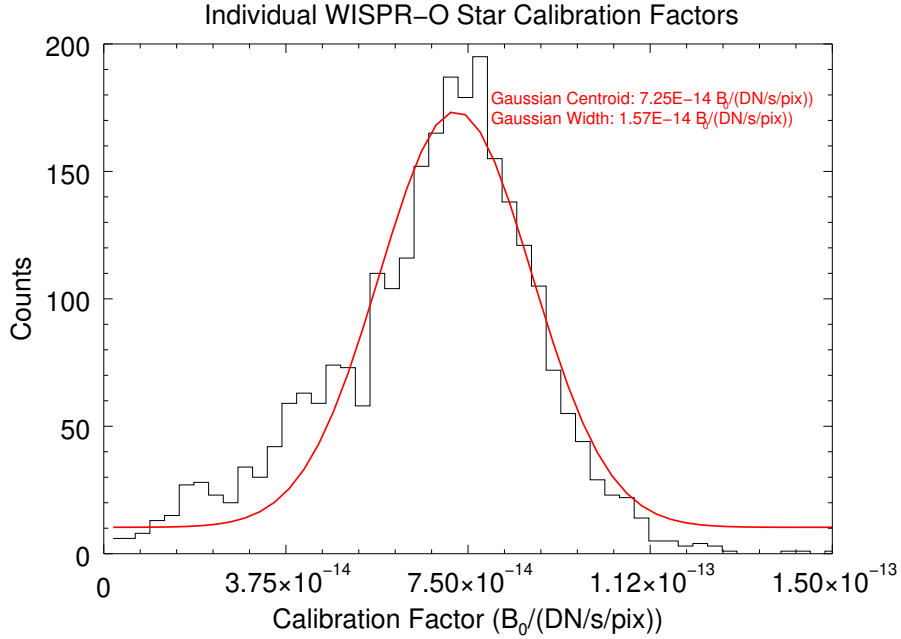


**Figure 18.** This histogram features every star (counts) from Figure 17, with a calibration factor determined individually by dividing the observed brightness by the expected brightness. The red line is a Gaussian fit of the data.

If further convincing is needed for the reliability of the coronal signal in WISPR-O based on the deviations from linearity in Figure 17, we point the reader to Stenborg *et al.* (2020), who was able to successfully match the intensity of the F-corona through both detectors. There are also no clear artifacts in the data resembling Figure 4. Given all this evidence, we feel confident that the data are accurate enough to lend themselves to any heliospheric study, though future refinement is possible.

## 7. Vignetting and Instrumental Artifacts

### 7.1. Vignetting Function

Vignetting is a variation of the throughput across the field of view. In the case of WISPR, both inner and outer telescopes present slight natural vignetting due to the optical design of the instrument. For WISPR-I, this is mostly due to the front aperture, that appears smaller for collimated light at large angles compared to the boresight. For WISPR-O the process is similar, except that the limiting aperture is internal so the vignetting effect is smaller. The vignetting images are shown in 19. They have been calculated using ray-tracing, based on the nominal lens prescription and mechanical design.

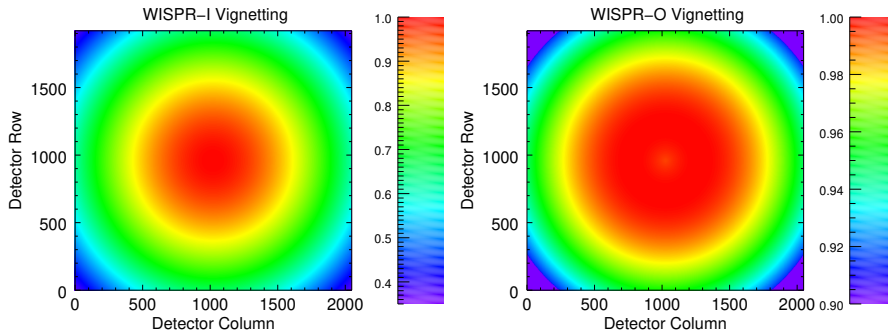


**Figure 19.** The vignetting functions for each of the WISPR telescopes.

In addition, the inner telescope shows some additional vignetting in the inner field of view. The vignettted area is along the inner field of view edge of the detector, the edge that sees closer to the Sun. The throughput is null at the edge of the detector and ramps up quasi-linearly up to the level of the natural vignetting around 2 degrees away from that inner edge. This vignetting is due to the last forward baffle partially occulting the objective lens. The function of the forward baffles is to further attenuate the sunlight diffracted by the edge of the spacecraft Thermal Protection Shield (TPS). The TPS is the first of the forward baffles in the attenuation of the direct sunlight. Currently, this vignetting is not corrected for in the L2 pipeline, though is something we hope to quantify and address in the future.

## 7.2. Stray-Light

The photospheric light diffracted at the edges of the baffles results in a constant brightness term across the FOV of the WISPR telescopes, its level being a function of the heliocentric distance of the PSP S/C. Hereafter, we refer to this term simply as “stray-light“ (or SL).

To determine the overall contribution of this unwanted source, Stenborg *et al.* (2020) computed the location of the symmetry axis of the WISPR images for a comprehensive set of sampled images in orbits 1, 2, 4, and 5, and analyzed the brightness profile along them. In particular, they found that for WISPR-I all brightness profiles superposed onto each other regardless of the observer’s heliocentric distance and orbit, their radial gradients exhibiting an average slope of about  $-2.295 \pm 0.006$  when displayed in a log–log scale. They concluded, therefore, that the SL contamination in WISPR-I images is negligible, at least for the first five orbits (based on the absence of a component dependent on the observer’s location) and hence a SL correction not necessary. On the other hand, that was not the case for WISPR-O images (see Figure 3 in Stenborg *et al.*, 2020).

To estimate the overall brightness level of unwanted sources of each WISPR-O image, Stenborg *et al.* (2020) followed the traditional approach devised by Bohlin, Koomen, and Tousey (1971). As adapted to WISPR, the method they

employed consisted of matching the slope of the brightness profiles of WISPR-O images to that of the corresponding WISPR-I images. Details of the procedure can be found in Section 2.2 of Stenborg *et al.* (2020).

While for an image by image basis, it is possible to determine the SL level manually in the manner explained in Stenborg *et al.* (2020), this is a time consuming process and not practical for every WISPR-O image. When plotting the SL levels for a series of images taken at different radial distances, a clear trend between SL and radial distance was seen. This is shown a number of select images in Figure 20.

For the pipeline processing of the calibration of WISPR images, we used these manually determined SL values to develop a function that could accurately model the SL as a function of the spacecraft distance from the Sun. The best model found to describe the SL was found to be piece-wise, differing inside and outside 0.15 AU as follows

$$S(r) = \begin{cases} 0.75 \times 10^{-14} r^{-3} & \text{for } r \leq 0.15 \text{ AU} \\ 0.50 \times 10^{-13} r^{-2} & \text{for } r > 0.15 \text{ AU} \end{cases} \quad (4)$$

where  $S(r)$  denotes the SL model and  $r$  the heliocentric distance of the observer. The SL values of the images sampled and fitting functions used are displayed in Figure 20. The use of a piece-wise function inside and outside 0.15 AU is motivated by the stronger dependence of the SL component with the radial distance of the observer, as inferred from the empirically-obtained values.

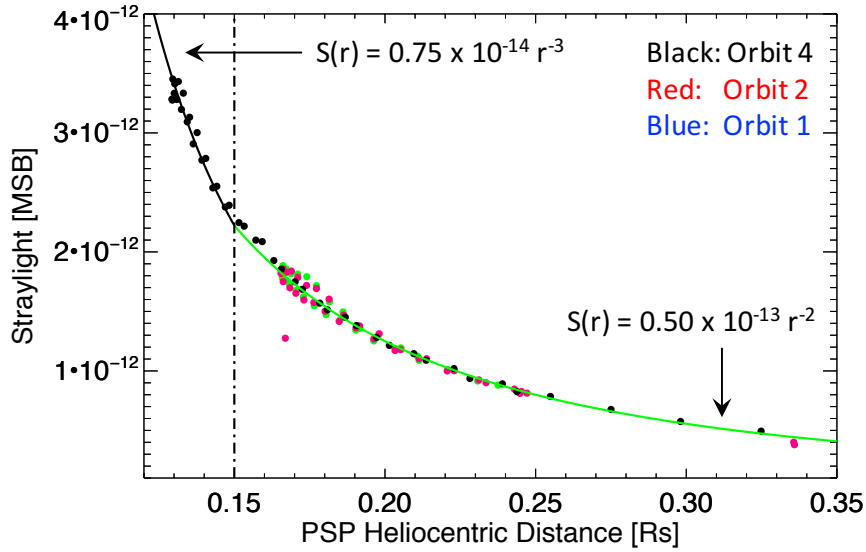


**Figure 20.** WISPR-O straylight values for a selected sample of images in orbits 1 (blue dots), 2 (red dots), and 4 (black dots). The green and black continuous lines delineate the straylight model  $S(r)$  (Equation 4).

For upcoming orbits, as PSP gets closer to the Sun, the degree of over-occluding lessens and therefore a correction to the SL model may be needed. We always anticipated that the instrumental component of the SL might change from orbit to orbit due to radiation damage or dust impacts on the objective lens. But, as can be seen in Figure 20, the SL values from the different orbits overlaid each other rather well, with no discernible trend, indicating that degradation of the lens through orbit 4 is minimal. We also do not see any temporal trend in the calibration factors derived from the stars.

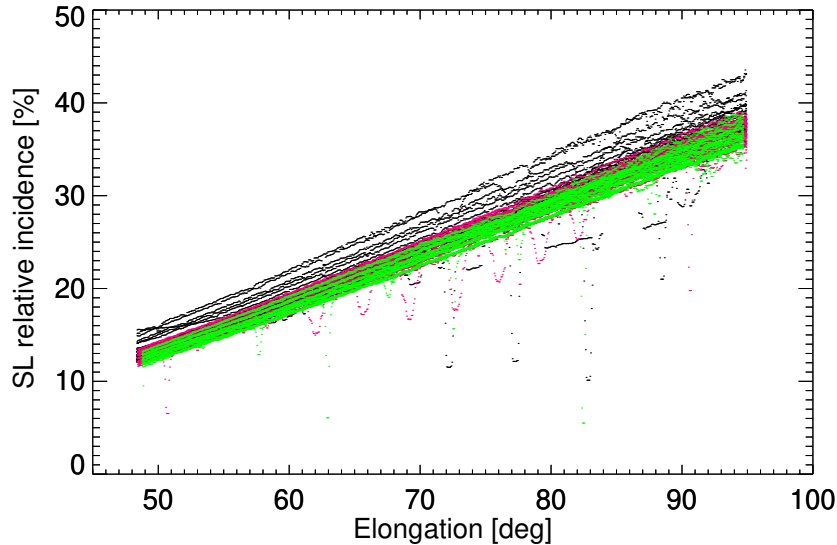


**Figure 21.** Relative incidence of the WISPR-O stray light values along the symmetry axis of the sampled images for orbits 1 (green), 2 (red), and 4 (black). The excursions below the average trend correspond to the passage of bright features (e.g., stars, stars clusters, planets).

In Figure 21 we show the relative incidence, meaning the fraction of the overall signal in an image represented by the SL term, of the SL values computed as a function of the elongation along the symmetry axis (in degrees) covered by WISPR-O for the sampled images in orbits 1 (blue), 2 (red), and 4 (black). We see that to match the WISPR-O radial gradients to those of WISPR-I, large values of SL relative to the overall signal are required. Due to the strong radial gradient of the signal (which falls off as  $r^{-2.3}$ ) we note that the relative incidence of the SL component varies from about 10% at the inner edge up to about 40% at the outer edge. For the SOHO/LASCO coronagraphs, the SL level is about 1% of the total brightness (e.g., Morrill *et al.*, 2006). Note however that the largest elongation covered by LASCO-C3 is about  $8^\circ$ .

Halain *et al.* (2011) examined the SL performance of the SECCHI/HI's and demonstrated a relatively stable SL level on the order of  $10^{-14}$  MSB in HI-1 and  $10^{-15}$  MSB in HI-2. The SL levels in WISPR for comparable elongations are significantly higher due to the spacecraft being much closer to the Sun. If we

extrapolate the model from Figure 20 to 1 AU, the SL value would be  $5 \times 10^{-14}$ , comparable to what was observed in the HIs. The higher SL caused by the near-Sun location of the spacecraft combined with the low overall signal at the largest elongations in WISPR-O cause the large relative incidence at the outer FOV of the telescope.

Another contribution to the SL values in the outer telescope is that in the region of space that WISPR-O is observing, the zodiacal light intensity becomes comparable to the diffuse galactic background (especially at the largest elongations). Thus, the galactic background adds a fixed contribution of a similar magnitude to the instrumental SL term. Our approach to estimate the SL values does not distinguish between the two (a single additive term enables the radial gradient to be linear over this wide range of elongations).

## 8. Summary

We have described the current status of the calibration of the two WISPR telescopes. The calibration procedures are very similar across the two telescopes, with some key differences. For an image to be classified as Level-2, all of the following corrections must be applied. This is true for all L2 data currently released. Because the L3 data are generated from released L2 files, these same corrections are also applied to the L3 files.

- **Bias Removal (Section 4.3):** The electronic bias of the APS detectors is manifested as a strong column-to-column variation in the detector. With the exception of some calibration images, the bias subtraction is performed on-board to improve the compression efficiency. However, to ensure that the on-board bias subtraction results in positive values, an offset term is applied that we remove as part of the image processing pipeline. Because the bias is typically removed on-board, this is applied even to the L1 images. But some images that aren't part of the normal, synoptic observing program and may therefore still have the bias, this can still be removed in the L2 pipeline. The offset term is only removed when processing the images to L2.
- **Linearity Correction (Section 4.2):** In high gain mode, the detectors are not quite linear. The deviation is typically small,  $\lesssim 1\%$ . However, when the exposure time changes, as it must do frequently throughout an encounter to properly resolve the corona at a given height, the non-linearity effects become noticeable. Using images taken before and after exposure time changes, an empirical correction was found for each detector and is applied to the images to reduce the effect throughout the orbit. This is an empirical correction of an artifact that is difficult to isolate, so it is likely that more data will lead to improvements in the future.
- **Stray-Light Removal (Section 7.2):** In the outer telescope, there is a noticeable background signal that is a combination of artificial stray-light and the galactic background. The latter is not an artifact, strictly speaking. For the purposes of studying the corona and heliosphere, however, the

galactic background needs to be removed. By matching the F-corona profile for co-temporal images along their photometric axis, a stray-light model as a function of radial distance was determined and this height dependent value is removed from each outer telescope image. As of now, because the signal in WISPR-I is so much brighter than that of WISPR-O, we do not believe there to be a noticeable stray-light/background contribution. However, we will continue to monitor this and may subtract a term off in the future.

- **Exposure Time Normalization:** Each image is divided by the total exposure time to normalize the signal in  $DN s^{-1}$  and provide a constant scale regardless of the exposure time.
- **Vignetting (Section 7):** Each image is divided by the vignetting function, which serves to increase the signal where the lens efficiency is low. The most notable region of vignetting is in the corner of each detector. Improvements to the vignetting based on the observations are one of the planned next steps for calibration updates.
- **Calibration Factor (Section 6):** Lastly the image is multiplied by the calibration factor,  $C_f$ , which converts the intensity into MSB units. This factor was initially estimated on the ground, but a more accurate value was determined using aperture photometry. For now, the data indicates that the calibration factor has been stable through each orbit. We will continue to test each orbit and see if any degradation of the instrument requires an update of the calibration factor.

Additionally, updates to the pointing and optical distortion model have been provided in the header (Section 5.2), allowing for the determination of physical coordinates in both heliospheric and celestial coordinate systems.

The L2 files are provided as data product on the WISPR website. Additionally, the WISPR\_PREP IDL routine, provided in the SolarSoft library (Freeland and Handy, 1998), can be used to turn any L1 image into an L2 image. Using WISPR\_PREP, individual corrections (i.e. the linearity correction or the conversion factor) can be turned off to create an image that is processed to an intermediate level between L1 and L2. This is useful if an individual user wants to study something closer to the raw photon counts on the detector without applying the calibration factor or exposure time normalization, but still apply some of the corrections for artifacts like linearity or the offset term.

These L2 images are used to determine image specific F-corona backgrounds (Level-2B) and background subtracted (Level-3) images (Stenborg, Hess, and Howard, 2021). These L3 images, also provided on the WISPR website, are the most useful representation of the K-corona in each image.

## 9. Conclusions

The results presented here should not be considered as the final WISPR calibration. Given the continually evolving mission profile that dictates changes to the observing strategy, we expect that several of the calibration steps will need to be updated and/or improved. If any calibration updates apply to data from prior

orbits, the data will be updated and re-released with a new version number to indicate clearly that these are new L2 and L3 data. The details of any calibration update will be described in subsequent publications, as necessary.

Overall, the calibrations of the two WISPR telescopes are consistent with each other, and appear to be stable over each encounter. Both pointing and photometry of each telescope has shown no variability or degradation so far. Therefore, we are confident in the photometric accuracy of the L2 images. The images can be used, in conjunction with data taken from other coronagraphs and heliospheric imagers, to address the open questions in our understanding of the corona and solar wind.

**Acknowledgments** We would like to thank the referee for many helpful suggestions to improve this article. Parker Solar Probe was designed, built, and is now operated by the Johns Hopkins Applied Physics Laboratory as part of NASA's Living with a Star (LWS) program (contract NNN06AA01C). This work was supported by the NASA Parker Solar Probe Program Office for the WISPR program (contract NNG11EK11I). A.V. is supported by WISPR Phase E funds.

The authors have no conflicts of interest to declare that are relevant to the content of this article.

## References

- Battams, K., Knight, M.M., Kelley, M.S.P., Gallagher, B.M., Howard, R.A., Stenborg, G.: 2020, Parker Solar Probe Observations of a Dust Trail in the Orbit of (3200) Phaethon. *ApJ Supplemental Series* **246**(2), 64. DOI. ADS.
- Bewsher, D., Brown, D.S., Eyles, C.J.: 2012, Long-Term Evolution of the Photometric Calibration of the STEREO Heliospheric Imagers: I. HI-1. *Solar Physics* **276**(1-2), 491. DOI. ADS.
- Bohlin, J.D., Koomen, M.J., Tousey, R.: 1971, Rocket-Coronagraph Photometry of the 7 March, 1970 Corona from 3 to 8.5  $R_s$  (Papers presented at the Proceedings of the International Symposium on the 1970 Solar Eclipse, held in Seattle, U. S. A. , 18-21 June, 1971.). *Solar Physics* **21**(2), 408. DOI. ADS.
- Brown, D.S., Bewsher, D., Eyles, C.J.: 2009, Calibrating the Pointing and Optical Parameters of the STEREO Heliospheric Imagers. *Solar Physics* **254**(1), 185. DOI. ADS.
- Calabretta, M.R., Greisen, E.W.: 2002, Representations of celestial coordinates in FITS. *Astronomy & Astrophysics* **395**, 1077. DOI. ADS.
- Colaninno, R.C., Howard, R.A.: 2015, Update of the Photometric Calibration of the LASCO-C2 Coronagraph Using Stars. *Solar Physics* **290**(3), 997. DOI. ADS.
- Fox, N.J., Velli, M.C., Bale, S.D., Decker, R., Driesman, A., Howard, R.A., Kasper, J.C., Kinnison, J., Kusterer, M., Lario, D.: 2016, The Solar Probe Plus Mission: Humanity's First Visit to Our Star. *Space Science Review* **204**(1-4), 7. DOI. ADS.
- Freeland, S.L., Handy, B.N.: 1998, Data Analysis with the SolarSoft System. *Solar Physics* **182**(2), 497. DOI. ADS.
- Gardès, B., Lamy, P., Llebaria, A.: 2013, Photometric Calibration of the LASCO-C2 Coronagraph over 14 Years (1996 - 2009). *Solar Physics* **283**(2), 667. DOI. ADS.
- Halain, J.-P., Eyles, C.J., Mazzoli, A., Bewsher, D., Davies, J.A., Mazy, E., Rochus, P., Defise, J.M., Davis, C.J., Harrison, R.A., Crothers, S.R., Brown, D.S., Korendyke, C., Moses, J.D., Socker, D.G., Howard, R.A., Newmark, J.S.: 2011, Straylight-Rejection Performance of the STEREO HI Instruments. *Solar Physics* **271**(1-2), 197. DOI. ADS.
- Hess, P., Rouillard, A.P., Kouloumvakos, A., Liewer, P.C., Zhang, J., Dhakal, S., Stenborg, G., Colaninno, R.C., Howard, R.A.: 2020, WISPR Imaging of a Pristine CME. *ApJ Supplemental Series* **246**(2), 25. DOI. ADS.
- Howard, R.A., Moses, J.D., Vourlidas, A., Newmark, J.S., Socker, D.G., Plunkett, S.P., Korendyke, C.M., Cook, J.W., Hurley, A., Davila, J.M.: 2008, Sun Earth Connection Coronal and Heliospheric Investigation (SECCHI). *Space Science Review* **136**(1-4), 67. DOI. ADS.

- Howard, R.A., Vourlidas, A., Bothmer, V., Colaninno, R.C., DeForest, C.E., Gallagher, B., Hall, J.R., Hess, P., Higginson, A.K., Korendyke, C.M., Kouloumvakos, A., Lamy, P.L., Liewer, P.C., Linker, J., Linton, M., Penteado, P., Plunkett, S.P., Poirier, N., Raouafi, N.E., Rich, N., Rochus, P., Rouillard, A.P., Socker, D.G., Stenborg, G., Thernisien, A.F., Viall, N.M.: 2019, Near-Sun observations of an F-corona decrease and K-corona fine structure. *nature* **576**(7786), 232. DOI. ADS.
- Howard, R.A., Vourlidas, A., Colaninno, R.C., Korendyke, C.M., Plunkett, S.P., Carter, M.T., Wang, D., Rich, N., Lynch, S., Thurn, A., Socker, D.G., Thernisien, A.F., Chua, D., al, et: 2020, The solar orbiter heliospheric imager (solohi). *A&A*. DOI. <https://doi.org/10.1051/0004-6361/201935202>.
- Howard, T.A., DeForest, C.E.: 2012, The thomson surface. i. reality and myth. *The Astrophysical Journal* **752**, 130. DOI.
- Janesick, J.R., Elliott, T., Andrews, J., Tower, J., Pinter, J.: 2013, Fundamental performance differences of CMOS and CCD imagers: part V. In: Widenhorn, R., Dupret, A. (eds.) *Sensors, Cameras, and Systems for Industrial and Scientific Applications XIV* **8659**, SPIE, ???, 1. International Society for Optics and Photonics. DOI. <https://doi.org/10.1117/12.2008268>.
- Kaiser, M.L., Kucera, T.A., Davila, J.M., St. Cyr, O.C., Guhathakurta, M., Christian, E.: 2008, The STEREO Mission: An Introduction. *Space Science Review* **136**(1-4), 5. DOI. ADS.
- Korendyke, C.M., Vourlidas, A., Plunkett, S.P., Howard, R.A., Wang, D., Marshall, C.J., Waczynski, A., Janesick, J.J., Elliott, T., Tun, S., Tower, J., Grygon, M., Keller, D., Clifford, G.E.: 2013, Development and test of an active pixel sensor detector for heliospheric imager on solar orbiter and solar probe plus. In: *Proceedings of the SPIE, Society of Photo-Optical Instrumentation Engineers (SPIE) Conference Series* **8862**, 88620J. DOI. ADS.
- Koutchmy, S., Lamy, P.L.: 1985, In: Giese, R.H., Lamy, P. (eds.) *The F-Corona and the Circum-Solar Dust Evidences and Properties (ir)*, 63. DOI. ADS.
- Morrill, J.S., Korendyke, C.M., Brueckner, G.E., Giovane, F., Howard, R.A., Koomen, M., Moses, D., Plunkett, S.P., Vourlidas, A., Esfandiari, E., Rich, N., Wang, D., Thernisien, A.F., Lamy, P., Llebaria, A., Biesecker, D., Michels, D., Gong, Q., Andrews, M.: 2006, Calibration of the Soho/Lasco C3 White Light Coronagraph. *Solar Physics* **233**(2), 331. DOI. ADS.
- Pickles, A.J.: 1997, VizieR Online Data Catalog: Spectrophotometric Atlas of Standard Stellar Spectra (Pickles 1985). *VizieR Online Data Catalog*, VII/102. ADS.
- Poirier, N., Kouloumvakos, A., Rouillard, A.P., Pinto, R.F., Vourlidas, A., Stenborg, G., Valette, E., Howard, R.A., Hess, P., Thernisien, A., Rich, N., Griton, L., Indurain, M., Raouafi, N.-E., Lavarra, M., Réville, V.: 2020, Detailed Imaging of Coronal Rays with the Parker Solar Probe. *ApJ Supplemental Series* **246**(2), 60. DOI. ADS.
- Rouillard, A.P., Kouloumvakos, A., Vourlidas, A., Kasper, J., Bale, S., Raouafi, N.-E., Lavraud, B., Howard, R.A., Stenborg, G., Stevens, M., Poirier, N., Davies, J.A., Hess, P., Higginson, A.K., Lavarra, M., Viall, N.M., Korreck, K., Pinto, R.F., Griton, L., Réville, V., Louarn, P., Wu, Y., Dalmasse, K., Génot, V., Case, A.W., Whittlesey, P., Larson, D., Halekas, J.S., Livi, R., Goetz, K., Harvey, P.R., MacDowall, R.J., Malaspina, D., Pulupa, M., Bonnell, J., de Witt, T.D., Penou, E.: 2020, Relating Streamer Flows to Density and Magnetic Structures at the Parker Solar Probe. *ApJ Supplemental Series* **246**(2), 37. DOI. ADS.
- Stenborg, G., Howard, R.A.: 2017, A Heuristic Approach to Remove the Background Intensity on White-light Solar Images. I. STEREO/HI-1 Heliospheric Images. *The Astrophysical Journal* **839**, 68. DOI. <http://adsabs.harvard.edu/abs/2017ApJ...839..68S>.
- Stenborg, G., Hess, P., Howard, R.A.: 2021, Background Modeling and Science Data Exploitation of PSP/WISPR Observation. *Solar Physics* **submitted**.
- Stenborg, G., Howard, R.A., Stauffer, J.R.: 2018, Characterization of the White-light Brightness of the F-corona between 5° and 24° Elongation. *The Astrophysical Journal* **862**(2), 168. DOI. ADS.
- Stenborg, G., Howard, R.A., Hess, P., Gallagher, B.: 2020, PSP/WISPR Observations of Dust Density Depletion Near the Sun I. Remote Observations to 8 Rs from an Observer Between 0.13-0.35 AU. *Astron. Astrophys.* **862**(2), 168. DOI. ADS.
- Stetson, P.B.: 1987, DAOPHOT: A Computer Program for Crowded-Field Stellar Photometry. *Publications of the Astronomical Society of the Pacific* **99**, 191. DOI. ADS.
- Szalay, J.R., Pokorný, P., Bale, S.D., Christian, E.R., Goetz, K., Goodrich, K., Hill, M.E., Kuchner, M., Larsen, R., Malaspina, D., McComas, D.J., Mitchell, D., Page, B., Schwadron,

- N.: 2020, The Near-Sun Dust Environment: Initial Observations from Parker Solar Probe. *ApJ Supplemental Series* **246**(2), 27. DOI. ADS.
- Thernisien, A.F., Morrill, J.S., Howard, R.A., Wang, D.: 2006, Photometric Calibration of the Lasco-C3 Coronagraph Using Stars. *Solar Physics* **233**(1), 155. DOI. ADS.
- Thompson, W.T.: 2006, Coordinate systems for solar image data. *Astronomy & Astrophysics* **449**(2), 791. DOI. ADS.
- Vourlidas, A., Howard, R.A., Plunkett, S.P., Korendyke, C.M., Thernisien, A.F.R., Wang, D., Rich, N., Carter, M.T., Chua, D.H., Socker, D.G.: 2016, The Wide-Field Imager for Solar Probe Plus (WISPR). *Space Science Review* **204**(1-4), 83. DOI. ADS.
- Wenger, M., Ochsenbein, F., Egret, D., Dubois, P., Bonnarel, F., Borde, S., Genova, F., Jasniewicz, G., Laloë, S., Lesteven, S., Monier, R.: 2000, The SIMBAD astronomical database. The CDS reference database for astronomical objects. *Astronomy & Astrophysics Supplemental Series* **143**, 9. DOI. ADS.
- Wood, B.E., Hess, P., Howard, R.A., Stenborg, G., Wang, Y.-M.: 2020, Morphological Reconstruction of a Small Transient Observed by Parker Solar Probe on 2018 November 5. *ApJ Supplemental Series* **246**(2), 28. DOI. ADS.